Comparison of CFD and one-dimensional Bernoulli solutions of the flow in a plate and frame ultrafiltration module in Z configuration

Dal-Cin, M.M.; Darcovich, K.; Bourdoncle, M.; Kahn, Z.; Caza, D.

Publisher's version / Version de l'éditeur:
https://doi.org/10.1016/j.memsci.2005.05.31
Journal of Membrane Science, 268, pp. 74-85, 2006

Available online at www.sciencedirect.com
SCIENCE DIRECT
Journal of Membrane Science 268 (2006) 74–85
journal of MEMBRANE SCIENCE
www.elsevier.com/locate/memsci

Comparison of CFD and one-dimensional Bernoulli solutions of the flow in a plate and frame ultrafiltration module in Z configuration☆

Mauro M. Dal-Cin[a,*], Ken Darcovich[a], Mathieu Bourdoncle[b], Zahra Khan[a], Daniel Caza[a]

[a] *National Research Council of Canada, Institute for Chemical Process and Environmental Technology, Ottawa, Ont., Canada K1A 0R6*
[b] *ICAM-Toulouse, 75, av. de Grande Bretagne, 31300 Toulouse, France*

Received 24 December 2004; received in revised form 20 May 2005; accepted 25 May 2005
Available online 24 August 2005

Abstract

Predictions of flow and pressure distributions in one bank of a plate and frame ultrafiltration module with five channels in parallel operating in a Z configuration were predicted using (1) Bernoulli's equation and a momentum balance in one dimension and (2) a three-dimensional field solution (Computational Fluid Dynamics) of the Navier-Stokes equation. CFD solutions were taken as the benchmark and used to refine the 1D model being developed to evaluate flow and pressure distributions for different operating conditions and ultimately different module configurations. The 1D model was able to provide quantitatively accurate flow distribution and qualitatively representative pressure distributions. Flow distributions increased monotonically with increasing channel number, maximum/minimum flow ratios in channels increased from 2 to 6.9 with oil ($\mu = 0.0361\,\mathrm{kg/m/s}$) as the design cross flow velocity increased from 0.5 to 5 m/s. Pressure distributions were well predicted qualitatively but were typically 40% lower than the CFD solution in the distributor. Key to the accuracy of the 1D model were the implementation of (a) variable contraction co-efficients in the distributor orifice, (b) the 1/7th power law for velocity profiles in the plenums (c) a new approach for combining flows in the collector and (d) assuming only one half of the orifice area was being effectively used by the fluid.

Keywords: Computational fluid dynamics; Modeling; Flow distribution; Pressure distribution; Ultrafiltration

1. Introduction

This study was motivated by a former collaborator who used an industrial scale plate and frame ultrafiltration module to process used motor oils. The overall bank productivity did not change as anticipated based on pressure limited flux or mass transfer limited flux using film theory when the operating pressure or pumping rates were changed; it was suspected that flow and pressure maldistribution in the five channels may have been a contributing factor. The current work represents the development of a 1D model which can give pressure and flow distributions for this and other module configurations. Three-dimensional field solutions (CFD) of the Navier-Stokes equations were used as a benchmark.

Distributed or partitioned flow systems are common in industrial practice. In spite of this, there exists only a small amount of technical data and theory available in the literature describing flow distribution behaviour in plate and frame systems. It is thus an objective of this paper to develop and present two approaches to modeling flow distribution in a plate and frame system, and to discuss their relative merits.

A finite-difference model developed by Majumdar [1] to resolve flow through dividing and combining manifolds was presented. The model was a mixed type, based on a one-dimensional momentum equation and flux continuity for flow along the axis of the distributor, and a Bernoulli type energy balance for velocity components and static pressure in the lateral direction. A characteristic pressure increase in the

☆ NRC No. 47850, originally presented in poster form at the 15th Annual Meeting of the North American Membrane Society meeting, June 26–30, 2004, Honolulu, Hawaii, USA.

* Corresponding author. Tel.: +1 613 993 0415; fax: +1 613 941 2529.
E-mail address: mauro.dal-cin@nrc-cnrc.gc.ca (M.M. Dal-Cin).

0376-7388/$ – see front matter © 2005 Elsevier B.V. All rights reserved.
doi:10.1016/j.memsci.2005.05.031

axial direction of the manifold was predicted, arising from the deceleration of the feed as fluid was bled off into the outlet streams. The dividing and combining manifolds were not coupled to form a closed system.

Heggs and Scheidat [2] studied the heat transfer and fluid distribution in a 60 channel plate and frame heat exchanger with a Z flow arrangement. Their 1D solution predicted a skewed parabolic flow distribution which, compared to a uniform distribution, varied from −45% at the first channel, to 200%, at the last channel. The lowest flow rate was located near the inlet but not at the first channel. Similar results were reported by Edwards et al. [3]. Kee et al. [4] proposed a generalized model for flow distribution in planar fuel cells, predicting uniform, parabolic or monotonically increasing flow distributions with channel number as a function of dimensionless module and operating parameters.

A three-dimensional solution was sought using the commercial CFD code, Fluent©. The 3D solution produced high resolution pressure and velocity fields which provided a basis for evaluating the appropriateness and quantitative accuracy of some of the engineering expressions employed in Bernoulli-type models. Naturally, a sufficiently accurate simple mathematical model is preferable for engineering work. The corresponding full Navier-Stokes simulation results are used to validate the simpler 1D solution. The latter can then be used as a screening tool for optimization of module designs.

New contributions in this work to the 1D solution, which were not implemented in the preceding references, were (1) incorporation of the 1/7th power law velocity distribution in the distributor and collector, (2) use of a variable contraction co-efficient for distributor orifice pressure drops and (3) a unique approach to model combining flows in the collector.

Solutions to the 1D problem were obtained using an electric circuit analogue. This approach has been used to model the circulatory system of the human body, where, for example, a capacitor was used to represent the elasticity of the blood vessels [5,6]. Toldy et al. [7] and Ke and Ti [8] used a similar approach to model pipeline flow.

The present work deals with the flow field in only one bank of the total module. It assumes that an inlet manifold, which was omitted for the present work, provides equal distribution to all three bank inlets. Future work will seek to model the main inlet manifold, attempt to optimize physical parameters of the module and address permeation behaviour. Aspects regarding the impact of inter-channel maldistribution are discussed qualitatively in the current work.

2. The physical system

The plate and frame module consists of 10 banks with five channels per bank. Dimensions and other details are given in Table 1. A schematic of the flow path is given in Fig. 1; the main feed goes to a slot manifold which nearly spans the width of the module and feeds the three distributor tubes at the top of the bank. The distributors and collectors are formed by a series of co-linear openings in the plates. Membranes are fastened to the plates using circular clamps which also define the distributor and collector diameters, D_p, and the orifice diameter, d. The orifice area is defined by

$$A_o = \pi D_p h \quad (1)$$

where h is the channel gap. As will be discussed later, the 1D model uses a modification where the orifice area is assumed to be one half that given by Eq. (1). Only the orifice area is halved for the purposes of calculating orifice pressure losses, Dp is not changed.

Computational efficiency was gained by modeling one third of the channel width with the assumption of equal flow distribution to each of the three distributors. It is recognized that this may be a poor assumption, particularly for

Table 1
Design parameters of full scale stack and feed properties

Component	Dimension
Feed inlet/outlet diameter	0.0762 m (3 in.)
Inlet manifold	0.0762 × 0.356 × 0.0127 m (3 × 14 × 0.5 in.)
Number of collectors/distributors	3
Collector/distributor diameter, D_p	0.0349 m (1.375 in.)
Channel gap, h	0.00635 m (0.25 in.)
Number of channels per bank, n	5
Number of banks	10
Channel width, w	0.4 m
Channel length, l	1.3 m (1.2 m distributor to collector centers)
Plate thickness, L_p	0.0635 m (0.25 in.)
Viscosity, μ (@ 70°)	0.036 kg/m/s
Density, ρ	880 kg/m^3

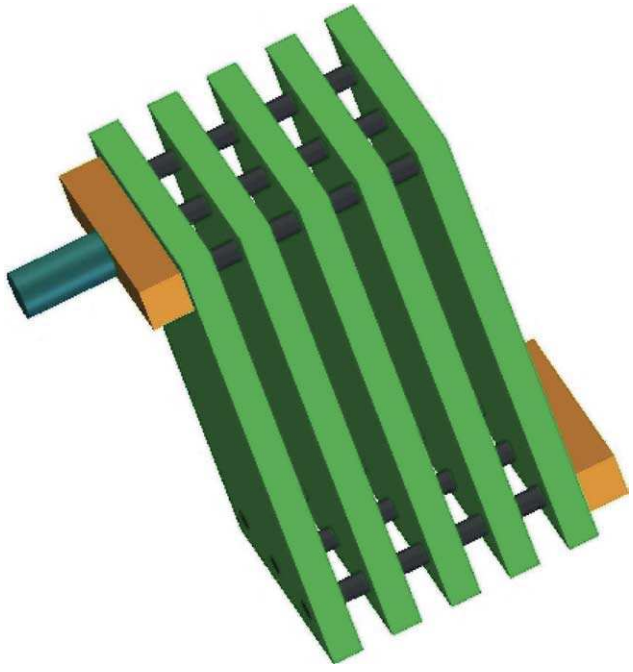

Fig. 1. Flow volume of retentate in the first bank, showing main inlet tube and manifold.

the first bank immediately following the main inlet manifold, but may be more appropriate for subsequent banks. Modeling was further simplified with the assumption of a solid wall for the membrane surfaces as the fluxes were considered negligible. Average fluxes with used motor oil as the feed were $< 3\,l/m^2/h$ ($4.16 \times 10^{-6}\,m^3/s$), with a permeation area of approximately $5\,m^2$ per bank, this flux is only 0.032% of the feed rate. Karode [9] showed that deviations from pressure drops for impermeable walls only became significant with module lengths well beyond those in the plate and frame module and with significantly higher fluxes ($100\,l/m^2/h$).

3. Theory

3.1. 1D model

3.1.1. General description and solution method

Flow and pressure distributions in 1D were obtained using an electric circuit analogue, a typical circuit is shown in Fig. 2. Flow directions are assumed to be left to right and top to bottom, in the direction of increasing channel number and from the inlet to the outlet. The volumetric flow rate and the pressure are analogous to the current and voltage, respectively.

The 1/7th power law velocity profile was assumed in the distributor and collectors. It was also assumed that this profile re-established itself immediately after the perturbations arising from branching and combining flows after each of the channels. Fluid at the circumference with the subscript c represents fluid leaving the distributor or entering the collector. The subscript r designates fluid which (a) remains in the distributor and continues downstream or (b) is coming from upstream in the collector.

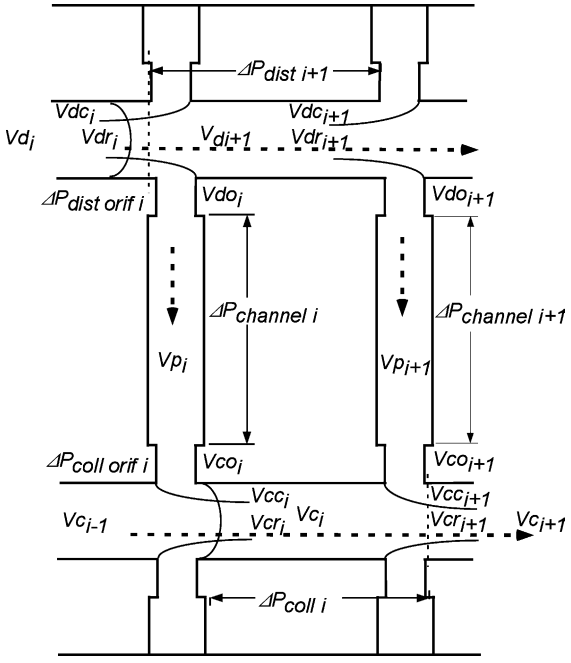

Fig. 2. Schematic of flow loop for the ith and $(i+1)$st channels, dashed arrows indicated assumed flow direction.

Starting immediately after orifice i in Fig. 2, the clockwise pressure balance around the loop defined by channels i and $i+1$ is,

$$\Delta P_{d_{i+1}} + \Delta P_{do_{i+1}} + \Delta P_{channel_{i+1}} + \Delta P_{co_{i+1}} - \Delta P_{c_i} - \Delta P_{co_i} - \Delta P_{channel_i} - \Delta P_{do_i} = 0 \quad (2)$$

The positive terms in Eq. (2) represent pressure changes in the assumed clockwise flow direction for the $(i+1)$st distributor, distributor orifice, channel and collector orifice. The negative terms represent pressure changes opposite the assumed flow direction for the ith collector, collector orifice, channel and distributor orifice. The solution was obtained by varying the volumetric flow rate in each channel such that the function PE, which we called the pressure error, PE:

$$\mathrm{PE} = \sum_{i=1}^{n} (\text{Eq. } 2)^2 \quad (3)$$

was minimized. This forced the pressure loss for the fluid in channels i and $i+1$ and the associated collector and distributor to be equal, as they must be, under the assumption of no pressure change across the diameter of the distributor or collector. There are $n-1$ unknown flows in the n channels, the last being known by conservation of mass.

Initial guesses of equal flow distributions were used. The appropriate pressure loss expressions for laminar or turbulent conditions were used depending on the local Reynolds number. The Reynolds numbers of interest in the module are for the plenums, orifices and channels (see Nomenclature), specific values for the various Reynolds numbers are discussed in the relevant sections of the 1D model description. Issues regarding turbulent-laminar flow in the CFD solution are discussed in Section 3.2.6. The transition between laminar to turbulent flow with the 1D model occasionally caused premature convergence to an incorrect solution by some solver routines as this represented a constraint. A new initial guess, which caused the local conditions to cross over into the other flow regime, was used in these cases. A solution was typically obtained in less than 10 s and with $\mathrm{PE} < 1\,Pa^2$. The individual terms in Eq. (2) are described below.

3.1.2. Distributor losses

We will address two pressure changes in the distributor, one for the fluid leaving the distributor, $\Delta P_{do_{i+1}}$, and one for the fluid remaining in the distributor, $\Delta P_{d_{i+1}}$.

3.1.2.1. Distributor orifice losses. Bernoulli's energy equation for a single sharp edged orifice, $\Delta P_{do_{i+1}}$, according to

Strakey and Talley [10] is

$$\frac{P_{\mathrm{d}_i}}{\rho} + \frac{1}{2}V_{\mathrm{dc}_i}^2 - E_{\mathrm{turb}} - E_{\mathrm{fric}} = \frac{P_{\mathrm{do}_i}}{\rho} + \frac{1}{2}V_{\mathrm{do}_i}^2 \tag{4}$$

where V_{dc_i} is the average velocity of the fluid leaving the distributor from the circumference, V_{do_i} is the average velocity of the fluid in the orifice, P_{d_i} and P_{do_i} are the pressures in the distributor and at the orifice exit.

Frictional losses along the orifice wall are

$$E_{\mathrm{fric\ ori}} = 0.04\frac{e}{d}\frac{V_{\mathrm{do}_i}^2}{2} \tag{5}$$

where e and d are the orifice length and diameters respectively. Turbulent losses are determined using Strakey's solution of potential flow theory in an infinitely wide channel with a slot orifice. Strakey's dimensions for the slot "a" and manifold height "b" correspond to the channel gap, h, and 1/2 the distributor diameter, D_{p}, in our module. E_{turb} is

$$E_{\mathrm{turb}} = \frac{V_{\mathrm{do}_i}^2}{2}\left(\frac{1}{C_{\mathrm{c}}}\right)^2(1 - C_{\mathrm{c}})^2. \tag{6}$$

Strakey showed that for $e/h > 1$, the contraction coefficient, C_{c}, was a function of only $V_{\mathrm{do}_i}/V_{\mathrm{dc}_i}$ and reached the limiting value of 0.61 if $V_{\mathrm{do}_i}/V_{\mathrm{dc}_i} > 2$. The C_{c} in the manifold problem of Darcovich et al. [11] was set at a constant (~ 0.61). The typical situation in the plate and frame module did not allow this assumption as V_{do_i} was typically $< V_{\mathrm{dc}_i}$ which gave C_{c} values as low as 0.15, and represented almost 2 orders of magnitude difference in the orifice pressure drop.

The C_{c} is normally calculated by solving four simultaneous non-linear equations. 1D solutions were facilitated by expressing C_{c} as a function of only $V_{\mathrm{do}_i}/V_{\mathrm{dc}_i}$ since the ratio e/h was constant and equal to 2 for this module. A nonlinear regression of the functional form of Eq. (7) with exact solutions to Strakey's potential flow theory yielded

$$C_{\mathrm{c}} = 0.61\left(1 - \exp\left(\frac{-1.5058V_{\mathrm{do}_i}}{V_{\mathrm{dc}_i}}\right)\right). \tag{7}$$

Typical engineering calculations assume a uniform velocity profile in a pipe in turbulent flow [12]. This will underestimate the pressure increase along the distributor, particularly at higher mean cross flow velocities. A flat velocity profile also gives larger values for $V_{\mathrm{do}_i}^2$ which overestimates orifice pressure losses in Eq. (6). The 1/7th power law velocity profile was incorporated in this work using the approach of Escobar [13] and Darcovich et al. [11] for the distributors and, in a new approach, was extended to the collector. Reynolds numbers in the distributor, which represents the upstream condition for the orifice, are 1800 for oil at the lowest cross flow velocity. Although the average distributor velocity decreases as flow exits via the channels the flow will be considered turbulent due to the short (0.00635 m) flow path before the next channel.

Implementation of the 1/7th power law velocity distribution required integrating the velocity profile:

$$\frac{Q_r}{Q_t} = 2\left(\frac{60}{49}\right)\left[\frac{49}{120} + \frac{7}{120}\frac{r}{R} - \frac{7}{15}\left(\frac{r}{R}\right)^2\right]\left(1 - \frac{r}{R}\right)^{1/7}, \tag{8}$$

which gives the fractional volumetric flow leaving the distributor, via the outer annulus, as a function of the radius. In any given iteration, the local Q_r/Q_t for the distributor in question was known based on the current flow distribution. The solution to Eq. (8) was expressed as a fifth order polynomial fit of Q_r/Q_t to give r. The average velocities of the fluid leaving via the orifice and remaining in the distributor were then calculated.

A similar approach was used to calculate the velocities of the fluids combining at the collector. At a given iteration and collector location, the ratio of fluid entering the collector Q_r and the total flow after combining, Q_t, were known. The radius partitioning the downstream collector was used to calculate the velocities of the core and annular fluid.

3.1.2.2. Distributor plenum losses. Bernoulli's energy balance for fluid remaining in the distributor to give $\Delta P_{\mathrm{d}_{i+1}}$ is

$$\Delta P_{\mathrm{d}_{i+1}} = \frac{\rho}{2}\left(\left(V_{\mathrm{dr}_i}^2 - V_{\mathrm{d}_{i+1}}^2\right) - \left(V_{\mathrm{dr}_i} - V_{\mathrm{d}_{i+1}}\right)^2 - 0.184\,N_{Re}^{-0.2}\frac{L_{\mathrm{p}}}{D_{\mathrm{p}}}V_{\mathrm{d}_{i+1}}^2\right) \tag{9}$$

where V_{dr_i} is the average velocity of the fluid remaining in the distributor after the ith channel and $V_{\mathrm{d}_{i+1}}$ is the average velocity of the same fluid after expanding. V_{dr_i} was determined using Eq. (8). The frictional losses are determined according to Geankopolis [14] where L_{p} and D_{p} are the plate thickness (which sets the fluid path length along the distributor in this configuration) and the distributor diameter.

3.1.3. Channel losses

The overall pressure drop in the ith flow channel, $\Delta P_{\mathrm{channel}_i}$, is estimated by

$$\Delta P_{\mathrm{channel}_i} = \Delta P_{\mathrm{entrance}} + \Delta P_{\mathrm{frictional}} + \Delta P_{\mathrm{contraction}} \tag{10}$$

The components of the overall channel pressure drop are summarized in Table 2 and depend on the Reynolds number in orifice or channel i. Channel Reynolds numbers were generally under 2000 with oil in all channels. The only exception was at a design cross flow velocity of 5 m/s in channels 4 and 5 where Re reached 2100 and 2700, respectively. Reynolds numbers with water indicated turbulent flow in all cases except in channel 1 at design cross flow velocities of 0.5 and 1 m/s where the maldistribution was such that these channels saw little flow.

The entrance/expansion losses are based on the orifice Reynolds number $= 2Dh_{\mathrm{orifice}}\rho V_{\mathrm{do}_i}/\mu$ calculated just

Table 2
Pressure drop contributions to flow in the channel for laminar and turbulent conditions

Pressure loss term	Laminar	Turbulent
$\Delta P_{\text{expansion}}$	$\frac{\rho}{2}\left(V_{o_i}^2 - V_{s_i}^2\right) - \frac{h}{L}(0.42 + 0.0281 N_{Re})\Delta P_s$	$\frac{\rho}{2}\left(V_{o_i}^2 - V_{s_i}^2\right) - \frac{\rho}{2}\left(V_{o_i} - V_{s_i}\right)^2$
$\Delta P_{\text{channel}}$	$12\, L\mu V_{s_i}/h^2$	$4 \times \frac{\rho}{2} 0.0868 N_{Re}^{-0.25} \frac{L}{D_h} V_{s_i}^2$
$\Delta P_{\text{contraction}}$	See text	$\frac{\rho}{2}\left[\left(V_{s_i}^2 - V_{o_i}^2\right) - K_c V_{o_i}^2 - 0.04\frac{e}{d} V_{o_i}^2\right]$

upstream of the channel. For oil cases, the orifice Reynolds numbers showed transitions from laminar to turbulent depending on the channel number and nominal design cross flow velocity as follows: at 2 m/s in channel 4, at 3 m/s in channel 3 and at 5 m/s in channel 2. Reynolds numbers with water were greater than 2000 for all channels and cross flow velocities. In laminar conditions the expansion loss is expressed as an equivalent length of the channel loss, where the constants 0.42 and 0.0281 are theoretical values for high aspect ratio channels [15]. Turbulent entrance/expansion losses are given by the Borda-Carnot equation where V_{s_i} is the average cross flow velocity in the channel.

Pressure drops under laminar conditions are given by the Hagen-Poiseuille flow analogue for channel flow. Turbulent friction losses use the Blasius equation for the friction factor f, where $2000 < N_{Re} < 10^5$ with the appropriate hydraulic radius. The contraction/exit losses for laminar conditions is usually expressed as an equivalent length of the downstream channel. In this situation, however, there is no downstream channel. In its place, a turbulent contraction is assumed for all cases.

3.1.4. Collector losses

The collector pressure loss, ΔP_{c_i}, comprises a pressure drop for (a) the orifice flow into the collector and (b) contraction and frictional losses.

3.1.4.1. Collector orifice losses. In lieu of a rigorous derivation of orifice losses for a collector analogous to Strakey's solution for the distributor, the orifice loss in the collector as estimated by Bernoulli's equation for the orifice pressure drop is:

$$\frac{P_{c_i}}{\rho} + \frac{1}{2}V_{cc_i}^2 - E_{\text{turb}} - E_{\text{fric}} - E_{\text{turning}} = \frac{P_{co_i}}{\rho} + \frac{1}{2}V_{co_i}^2 \tag{11}$$

Application of Strakey's method for the turbulent loss term is not appropriate in this situation. In its place, a turbulent contraction, turning loss and frictional component are used. The contraction loss is given by $K_c V_{cc_i}^2/2$ where V_{cc_i} is the fluid velocity in the outer annulus of the collector, estimated using Eq. (8) with the current estimates of the volumetric flow rates. The contraction coefficient, K_c, is estimated from a polynomial regression of tabulated values from [15]. The turning loss term is simply $V_{cc_i}^2/2$ typical of a 90° elbow.

3.1.4.2. Collector plenum losses. The fluid in the collector, after the ith channel has a velocity V_{cc_i}. As it approaches the $(i+1)$st channel it is forced into a smaller cross sectional area and accelerates to $V_{cr_{i+1}}$. As with previous dividing flows, the fluid velocity in the core can be estimated from Eq. (8).

Bernoulli's equation for the flow in the plenum is

$$\frac{P_{c_i}}{\rho} + \frac{1}{2}V_{c_i}^2 - E_{\text{turb}} - E_{\text{fric}} = \frac{P_{c_{i+1}}}{\rho} + \frac{1}{2}V_{cc_{i+1}}^2 \tag{12}$$

The frictional term is given by Geankopolis's expression using V_{c_i}. Reynolds numbers based on the average velocity in the collector were usually laminar after the first channels, a result of the maldistribution generating little flow in the collector until the channels near the end of the bank. Nonetheless flow was assumed turbulent owing to the constant influx of new flow from the channels and the short flow paths.

3.2. 3D simulation

3.2.1. Governing equations

The flow system was governed by equations conserving mass and momentum. At low Reynolds numbers this means respectively that the standard continuity and Navier-Stokes equations were employed. These are given below in Eqs. (13) and (14).

$$\frac{\partial \rho}{\partial t} + \nabla \cdot (\rho \vec{v}) = 0 \tag{13}$$

Eq. (13) is the general form of the mass conservation equation and is valid for incompressible as well as compressible flows.

Conservation of momentum in an inertial (non-accelerating) reference frame is given by,

$$\frac{\partial}{\partial t}(\rho \vec{v}) + \nabla \cdot (\rho \vec{v}\vec{v}) = -\nabla p + \nabla \cdot (\bar{\bar{\tau}}) + \rho \vec{g} \tag{14}$$

where p is the static pressure, $\bar{\bar{\tau}}$ is the stress tensor (described below), and $\rho\vec{g}$ is the gravitational body force.

The stress tensor $\bar{\bar{\tau}}$ is given by

$$\bar{\bar{\tau}} = \mu\left[(\nabla \vec{v} + \vec{v}^{\mathrm{T}}) - \frac{2}{3}\nabla \cdot \vec{v} N\right] \tag{15}$$

where μ is the molecular viscosity, N is the unit tensor, and the second term on the right hand side is the effect of volume dilation.

For elevated Reynolds numbers where turbulent flow occurs, additional equations are added to the system to

account for the extra complexity. Given the comparatively low Reynolds number turbulence and transition zones which occurred in the present system, the RNG-based k–ϵ turbulence model was selected. This model is derived from the instantaneous Navier-Stokes equations, using a mathematical technique called "renormalization group" (RNG) methods. The analytical derivation results in a model with constants different from those in the standard k–ϵ model, and additional terms and functions in the transport equations for k and ϵ. A more comprehensive description of RNG theory and its application to turbulence can be found in [16].

The RNG k–ϵ model has transport equations in a similar form to the standard k–ϵ model. They are written below in Eqs. (16) and (17):

For k,

$$\frac{\partial}{\partial t}(\rho k) + \frac{\partial}{\partial x_i}(\rho k u_i) = \frac{\partial}{\partial x_j}\left(\alpha_k \mu_{\text{eff}} \frac{\partial k}{\partial x_j}\right) + G_k + G_b - \rho\epsilon - Y_M \tag{16}$$

And for ϵ,

$$\frac{\partial}{\partial t}(\rho \epsilon) + \frac{\partial}{\partial x_i}(\rho \epsilon u_i) = \frac{\partial}{\partial x_j}\left(\alpha_\epsilon \mu_{\text{eff}} \frac{\partial \epsilon}{\partial x_j}\right) + C_{1\epsilon}\rho\frac{\epsilon}{k}(G_k + C_{3\epsilon}G_b) - C_{2\epsilon}\rho\frac{\epsilon^2}{k} \tag{17}$$

In these equations, G_k represents the generation of turbulence kinetic energy due to the mean velocity gradients and G_b is the generation of turbulence kinetic energy due to buoyancy. Y_M represents the contribution of the fluctuating dilation in compressible turbulence to the overall dissipation rate. The quantities α_k and α_ϵ are the inverse effective Prandtl numbers for k and ϵ, respectively.

The scale elimination procedure in RNG theory results in a differential equation for turbulent viscosity:

$$d\left(\frac{\rho^2 k}{\sqrt{\epsilon\mu}}\right) = 1.72\frac{\hat{\nu}}{\sqrt{\hat{\nu}^3 - 1 + C_\nu}}d\hat{\nu} \tag{18}$$

where

$$\hat{\nu} = \frac{\mu_{\text{eff}}}{\mu} \quad \text{and,} \quad C_\nu \approx 100$$

Eq. (18) is integrated to obtain an accurate description of how the effective turbulent transport varies with the effective Reynolds number (or eddy scale), allowing the model to better handle low Reynolds number, and near-wall flows.

In the high-Reynolds-number limit, Eq. (18) gives

$$\mu_t = \rho C_\mu \frac{k^2}{\epsilon} \tag{19}$$

with $C_\mu = 0.0845$, derived using RNG theory. It is interesting to note that this value of C_μ is very close to the empirically-determined value of 0.09 used in the standard k–ϵ model.

A number of the constants and parameters required for implementing the RNG model are outlined below. The inverse effective Prandtl numbers, α_k and α_ϵ, are computed using the following formula derived analytically by the RNG theory:

$$\left|\frac{\alpha - 1.3929}{\alpha_0 - 1.3929}\right|^{0.6321}\left|\frac{\alpha + 2.3929}{\alpha_0 + 2.3929}\right|^{0.3679} = \frac{\mu_{\text{mol}}}{\mu_{\text{eff}}} \tag{20}$$

where $\alpha_0 = 1.0$. In the high-Reynolds-number limit ($\mu_{\text{mol}}/\mu_{\text{eff}} \ll 1$), $\alpha_k = \alpha_\epsilon \approx 1.393$.

The main difference between the RNG and standard k–ϵ models lies in the additional term, R_ϵ, in the ϵ equation (Eq. (17)) given by,

$$R_\epsilon = \frac{C_\mu \rho \eta^3 (1 - \eta/\eta_0)}{1 + \beta\eta^3}\frac{\epsilon^2}{k} \tag{21}$$

where $\eta \equiv Sk/\epsilon$, $\eta_0 = 4.38$, $\beta = 0.012$. Above, 2 is the modulus of the mean rate of strain.

The model constants $C_{1\epsilon}$ and $C_{2\epsilon}$ in Eq. (17) have values derived analytically by the RNG theory. These values, used by default in Fluent© are,

$$C_{1\epsilon} = 1.42 \qquad C_{2\epsilon} = 1.68$$

These default values have been determined from experiments with air and water for fundamental turbulent shear flows including homogeneous shear flows and decaying isotropic grid turbulence. They have been found to work fairly well for a wide range of wall-bounded and free shear flows.

3.2.2. Boundary conditions

Boundary conditions specified at the inlet were a 1/7th power law velocity distribution and the corresponding turbulent kinetic energy and turbulent dissipation rate modeled after equations given in [17]. Concretely,

$$I = 0.16Re^{-1/8} \quad \ell = 0.07D_{\text{i}}$$
$$k = 1.5(Iu)^2 \qquad \epsilon = C_\mu \frac{k^{1.5}}{\ell}$$

Above, u is the fluid velocity normal to the inlet, I is the turbulence intensity, and ℓ is the turbulence mixing length, given in terms of the inlet diameter D_{i}.

At the outlet, the gauge pressure was specified to be 0 and the turbulent kinetic energy and turbulent dissipation rate were specified to be the same as at the inlet. Gravitational effects were applied in the vertical (x) direction.

3.2.3. Computational parameters

Convergence was verified by tracking (a) residuals (continuity, k, ϵ, and x, y, and z velocity components) (b) pressure distributions in the distributor and collector centerlines and (c) the average flow distribution in the channels. Pressure and flow distributions were examined at 1×10^{-3}, 1×10^{-4}, etc. for residuals. Pressure and flow distributions typically stabilized at convergence criteria of 1×10^{-4} or 1×10^{-5} for oil simulations and 1×10^{-5} or lower for water simulations.

Convergence was typically achieved after 500–1500 iterations with residuals unchanging for at least the final 100 iterations. A first-order downwind, segregated solver scheme was employed.

This simulation treated a system with sharp directional changes and severe geometry variations. In order to minimize convergence instabilities, relaxation factors between 0.5 and 0.15 were used. Periodic convergence behaviour was observed for larger relaxation factors.

3.2.4. Grid considerations

The grid was constructed in Gambit© by first meshing the channel faces (of all five channels) that surround the inlet and outlet tubes and then extending the mesh through the channel volume. Each face was meshed by defining nodes along all its edges and then allowing Gambit to map the mesh over the face. This was required in order to obtain a well-structured mesh. A short extension (0.0127 m or 2 channel widths) was added to the distributor at the inlet and collector outlet to avoid recirculation zones on the boundaries.

Each channel was divided into three zones for the purposes of meshing. The first zone extends from the top of the channel to 0.08 m past the center of the distributor. The mesh density in this zone is 0.09 cm to capture recirculation and turbulence effects. The second zone extends from the end of the first zone to 0.08 m before the center of the collector. The mesh density along the flow direction is 0.9 cm and along the channel gap and width it is 0.09 cm. The flow is fairly consistent in this region, so a less dense grid is able to give satisfactory results. The third zone makes up the rest of the channel in the vicinity of the collector and has the same mesh density as the first zone.

The grid densities employed gave pressure drop values accurate to within 5% for the range of laminar and turbulent Reynolds numbers treated in this work. These separate baseline tests were carried out on straight tubes.

It was only necessary to model one sixth of the actual structure in this simulation due to symmetry. The plane of symmetry lies at half the channel width along the y-axis after assuming perfect flow distribution to each of the distributors.

3.2.5. Run conditions

Five different runs were carried out for average cross flow velocities of 0.5, 1, 2, 3 and 5 m/s, assuming perfect distribution from the inlet manifold. The boundary conditions for turbulent kinetic energy and turbulent dissipation rate were set accordingly based on the diameter of the distributor.

Typical cross flow velocities in plate and frame modules are less than 1 m/s. Higher velocities were simulated to further validate comparisons between the 1D and CFD solutions. At lower cross flow velocities, the viscous losses in the channel dominated due to the high viscosity of the oil. This would not be a severe test for the pressure loss predictions of the distributor and collector using the 1D model. A further set of simulations was carried out with water (for its lower viscosity) at the same cross flow conditions to further reduce the contribution of the channel losses in comparison to the distributor and collector.

3.2.6. Turbulent to laminar transitions

From a trial calculation with oil at the highest mass flow rate, a value of $k = 14.66\,\mathrm{m^2/s^2}$ and $\epsilon = 1.3223 \times 10^4\,\mathrm{m^2/s^3}$ were extracted from a cell just below the feed tube in the center of the last channel. In a maldistributed bank, the last channel was found to have the highest flow rate through it. The ratio k/ϵ gives a characteristic time over which the turbulence should dissipate. When this characteristic time is multiplied by the average velocity in the channel, a characteristic length over which the turbulence will be eliminated can be estimated. For example, at an average fluid velocity of 5 m/s, the turbulence dissipation length was found to be 5.5 mm.

In some real cases however, because of flow maldistribution, the mass flow rate through the last channel at the 5 m/s nominal cross-flow velocity was found to be high enough to produce a turbulent channel Reynolds number. In particular the fourth and fifth channel for the highest inlet velocity case had turbulent flow.

In most cases, the Reynolds number of the flow in the channel indicated a laminar regime. Since no turbulence will be generated under these conditions, the parameters k and ϵ were found to decay quickly along the channel. Trial calculations indicated that for $Re < 500$, an essentially laminar character was output by the k–ϵ solver. In this way, the functionality of the turbulent parameters maintained a smoothness that would not be possible to achieve if laminar zones were imposed, which would necessarily entail some discontinuity in the solution of field variables. At present, Fluent© cannot support damping functions on turbulent properties.

4. Results and discussion

The aim of this work is to compare the flow and pressure distribution in a plate and frame module operating in Z configuration as predicted by both a 1D model and a CFD simulation. The CFD solutions were taken as the baseline to which the 1D solution was compared for identifying areas to improve the 1D model. An accurate 1D model would be suitable for rapid evaluation of module modifications. Changes to the 1D model which were implemented after analyzing the CFD solutions included:

- incorporation of the 1/7th power law velocity distribution in the collector,
- using a variable contraction co-efficient for the distributor orifice, and
- reduction of the effective orifice area.

Design cross flow velocities for plate and frame modules are typically 1 m/s or lower. However comparisons between the two models are carried out at much higher cross flow velocities to verify the accuracy of the 1D model. Flow and

pressure distributions were compared using water as a feed to further test the 1D model by reducing viscous effects in comparison to the oil feed.

4.1. 1D and CFD predictions: oil feed

Streamlines at the distributor, for an average cross flow velocity of 1 m/s, are shown in Fig. 3. An important feature observed at all cross flow velocities, is that the bulk of the flow goes down the channel, with very little flow above the distributor. This behaviour appears logical, but the degree to which this occurred was unexpected. Similar behaviour, not shown, was seen at the collector. This suggested that the 1D model could be modified with respect to the orifice dimensions. As an approximation, the orifice area at the distributor and collector orifices was halved based on the observations of the flow patterns. Halving the orifice area had relatively little impact on the overall pressure drop for a bank, but significantly altered the flow distribution to the channels.

A ratio of the maximum to minimum flow in any channel, κ, has been used as an overall measure of the maldistribution [18]. These results are summarized in Table 3 for the CFD, 1D half orifice and full orifice solutions. This simple measure can be misleading in cases where the flow in the first channel is very low, as in the 1D model using the full orifice area. The normalized flow rate in each channel is shown in Fig. 4. The

Table 3
Overall maldistribution, κ, for the CFD, 1D full orifice and 1D half orifice solutions for each cross flow velocity with oil

	Mean cross flow velocity (m/s)				
	0.5	1	2	3	5
Solution	κ				
1D full orifice	1.8	3.1	9.8	23.6	50.1
1D half orifice	1.8	2.7	4.5	6.4	8.2
CFD	1.7	2.3	3.6	5.0	6.9

CFD solutions are indicated by the solid lines while the 1D solutions using the half orifice area modification are shown by dotted lines. The normalized flow distributions in Fig. 4 are separated for visual clarity by shifting the curves in the y-direction by values of 0.5, 1, 1.5 and 2 for the 1, 2, 3 and 5 m/s design cross flow velocities respectively. Quantitatively the modified 1D and CFD solutions match well. Qualitatively the 1D solution always under predicts the curvature of the flow distribution, the trend increasing at higher cross flow velocities. The 1D flow maldistribution was over-predicted with the full orifice model (not shown for clarity).

The flow rate increases monotonically with increasing channel number. Previous 1D solutions [2,3] for the flow distribution in a similar geometry were parabolic with a minimum skewed towards the entrance. Similar distributions were

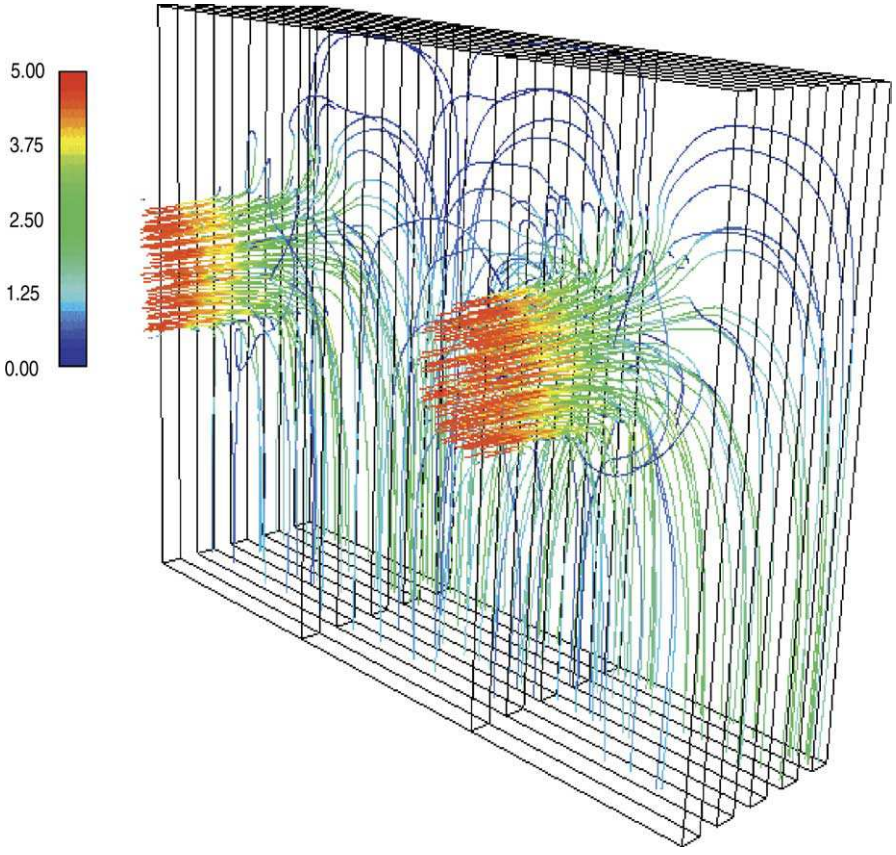

Fig. 3. Streamlines at the distributor for mean cross flow velocity of 1 m/s with oil.

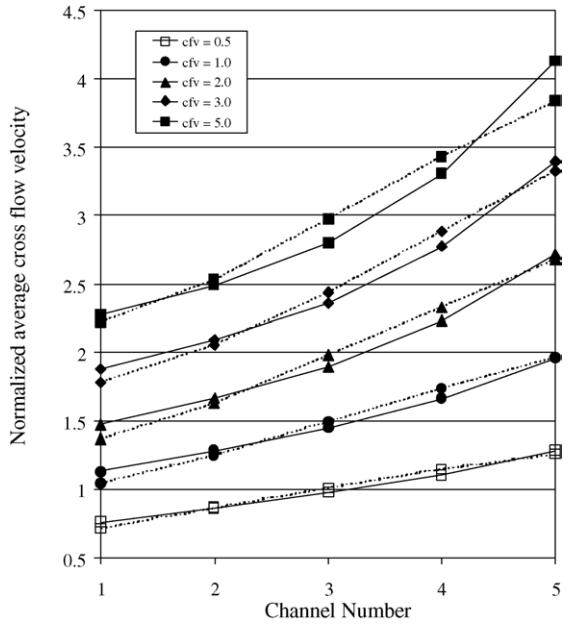

Fig. 4. Flow distributions for various mean cross flow velocities with oil. Solid lines represent CFD solutions, dotted lines represent 1D model solutions.

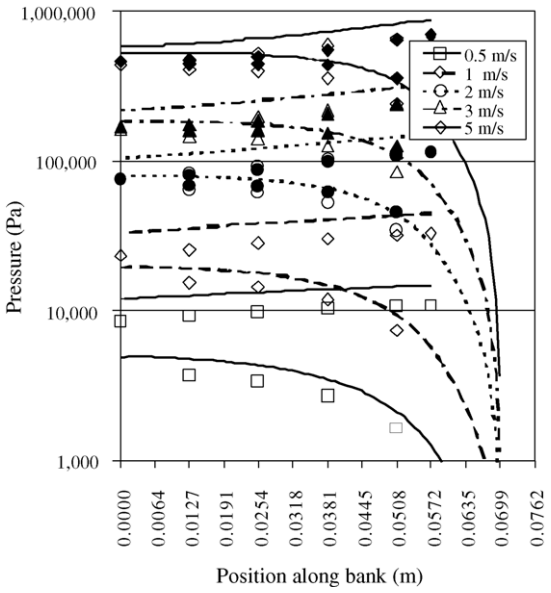

Fig. 5. Pressure distributions for various mean cross flow velocities with oil. CFD predictions for the distributor: upper line, collector: lower line. Solid symbols are for the 1D full orifice model, open symbols are for the 1D half-orifice model.

obtained with our 1D model before incorporating the 1/7th power law velocity profile in the distributor and collector. Using a flat velocity profile yields inaccurate predictions for (1) the orifice losses [10] and (2) underestimates the pressure increase along the distributor and pressure decrease along the collector.

Pressure distributions along the distributor and collector are shown in Fig. 5. Abscissa values are chosen such that each division represents the 0.00635 m increment of a channel or plate. The solid lines represent data from the CFD solution for each cross flow velocity along the plenum centerlines. The distributor is higher and the collector lower; decreasing to zero at the outlet. The 1D solution is indicated by symbols; the half orifice model using open symbols and the full orifice model using solid symbols. Differences in the pressure distributions between the full orifice and half orifice 1D models were not significant at the lower cross flow velocities.

The pressure increase along the distributor is the result of the decreasing velocity of the fluid, corresponding to the net flow rate decreasing as flow leaves the distributor into each channel. Likewise the pressure decrease in the collector towards the outlet is dominated by the velocity change due to incoming fluid. The last channel sees the highest distributor pressure and the lowest collector pressure, generating the greatest driving force for flow in that channel. The first channel sees the lowest distributor pressure and the highest collector pressure, generating the lowest driving force for flow in the channel at the inlet. This maldistribution of the pressure is exaggerated at higher cross flow velocities.

The 1D model qualitatively predicts the pressure distributions in the plenums. Quantitatively the 1D model underestimates the pressure values compared to the CFD solution by approximately 40% in the distributor. In the collector, the error is greatest at 0.5 m/s cross flow velocity (70% under predicted) and improves at the highest cross flow velocity to less than 10%.

Discrepancies in the pressure distribution for the two models may be due to the exit pipe used in the CFD grid to avoid recirculation at the boundary. If the 1D results in Fig. 5 are corrected for the pressure value at the end of the 1D model, or 0.05715 m, the error decreases to a maximum of 20% in either of the plenums. The correction was not applied because the 1D model assumes that steady state is achieved immediately after the flows have combined in the collector. For example, at the outlet, all losses are assumed to occur at the junction point at 0.0571 m, corresponding to the collector immediately after channel 5. The correction applied to the 1D model pressure values was the loss in the CFD predictions between 0.0571 m and 0.0699 m. However the loss in the extra exit tube in the CFD simulation represents losses which the 1D model has already accounted for, hence this correction should not be applied. At most a frictional loss, which was negligible, is the only correction which could be justified.

4.2. 1D and CFD predictions: water feed

Comparisons between the 1D models and CFD predictions using water were similar to those with oil. The 1D full orifice model over-predicted the maldistribution to a greater extent than with the oil; κ values were grossly different in this case, ranging from 231 to 943 compared to the CFD and 1D half orifice models (11–27), Table 4. Quantitatively, the flow distributions predicted by the 1D model, using the CFD as

Table 4
Overall maldistribution, κ, for the CFD, 1D full orifice and 1D half orifice solutions for each cross flow velocity with water

	Mean cross flow velocity (m/s)				
	0.5	1	2	3	5
Solution	κ				
1D full orifice	231	407	627	764	943
1D half orifice	11.1	12.9	15.2	16.6	18.5
CFD	17.8	21.5	24.3	25.5	27.2

the baseline, were not as accurate as with the oil simulations. Qualitatively, the maldistribution was under-predicted at the first and last channels by the 1D model, but the accuracy of the predictions could be considered acceptable for module design purposes.

Greater maldistribution with water is consistent with reported experimental and theoretical predictions of Edwards et al. [3]. Pressure losses in the channel act to equilibrate the flow in the channels. The lower viscosity of the water feed reduces this equilibration leading to greater maldistribution.

1D predictions of plenum pressure distributions with water (not shown) for the five cross flow velocities were similar to those of oil in Fig. 5. The inlet pressure predicted by the 1D model was 25–30% lower than the CFD solution at any of the cross flow velocities.

Overall pressure drops at the low cross flow velocities of 0.5 and 1 m/s were significantly lower with water as the feed compared to oil: 6.3 and 25.3 kPa for water compared to 11.9 and 32.7 kPa for oil, respectively. The channel losses represent a greater fraction of the overall pressure drop across the bank. At cross flow velocities of 2 m/s and higher; inviscid losses in the distributor, orifice and collector dominate for both fluids. The overall pressure drops were similar and marginally higher with water at 5 m/s due to its higher density. Frictional losses are minimal due to the short flow lengths in these portions of the bank.

4.3. Intra-channel flow distribution

Intra-channel flow distribution, or the velocity distribution across the width of the channel, is also important in determining module performance. A limitation of the 1D model as formulated is the absence of any such information. Velocity fields from the CFD solutions are shown for both oil and water in Fig. 6, left and right respectively, across the mid-gap of channels 1, 3 and 5 at 2 m/s.

The intra-channel maldistribution with oil became negligible shortly after entering the channel at the top. The maldistribution was greatest in channel 5, which had the greatest flow. When water was the feed, the intra-channel maldistribution was greater because of its lower viscosity. The ratio of the maximum to minimum velocity was 1.25, ignoring the wall boundary. This was negligible compared to the inter-channel maldistribution noted earlier, where $\kappa = 13.7$, Table 4.

4.4. Maldistribution and overall productivity

Changes in the overall productivity in a plate and frame membrane module will depend on the local conditions; if they are pressure or mass transfer limited. If the flux over the entire permeating area in the module is mass transfer limited then a very small reduction is predicted. The effect of maldistribution on the overall flux for a given bank of channels can be estimated by $\bar{k}'$, the overall mass transfer coefficient normalized by the mass transfer coefficient for perfect inter-channel flow distribution. Assuming $J_v \propto k^{1/3}$ and $k \propto= V^{1/3}$, the average cross flow velocity in a thin channel in laminar flow [19]:

$$\bar{k}' = \frac{\bar{k}}{k_{\text{ideal}}} = \frac{1}{n}\sum_{i=1}^{n}\left(\frac{V_i}{V_{\text{ideal}}}\right)^{0.33} \tag{22}$$

where $\bar{k}$ and k_{ideal} are the mass transfer coefficients for the overall stack and a channel with a cross flow velocity, V_{ideal}, corresponding to perfect inter-channel flow distribution.

Consider the reference case of two channels with cross-flow velocities of 1 m/s and fluxes of unity. If the maldistribution results in average cross flow velocities of 0.5 and 1.5 m/s (conserving the overall pumping rate) then $\bar{k}'$ and J_v would be 0.969. The lowest $\bar{k}'$, 0.93, was observed with water at 5 m/s based on the bulk flows. This is a negligible drop in performance for an extreme case of maldistribution if the flux was mass transfer limited. The reduced flux from one channel is compensated for by the increased flux in the other.

The impact of flow maldistribution on productivity becomes more significant if local conditions change between mass transfer and pressure limited flux.

An example is a situation where the flux is just mass transfer limited and then the recirculation rate is increased. The maldistribution will increase and the flux will become pressure limited in the last channel, in this case the flux increase may be less than that predicted by film theory and the flux in the front channels will not increase by the amount expected. The higher recirculation rate will also require a higher average pressure in the module and may partially oppose the transition to pressure limited flux.

The overall retention of solutes is potentially as important as the overall module productivity. If solutes are partially retained, the channels with lower cross flow velocities can see a lower retention. This will be governed by the local flux/mass transfer co-efficient (J_v/k) ratio and can be predicted from film theory. J_v/k will not dramatically increase as would be expected because the local flux will also be lower, if it is mass-transfer limited.

These are purely qualitative discussions on the impact of flow maldistribution. A rigorous analysis will be the subject of future work and is beyond the scope of this work. There are other practical considerations, cleaning protocols would not be as effective and critical velocities may be required to avoid deposition of particulates.

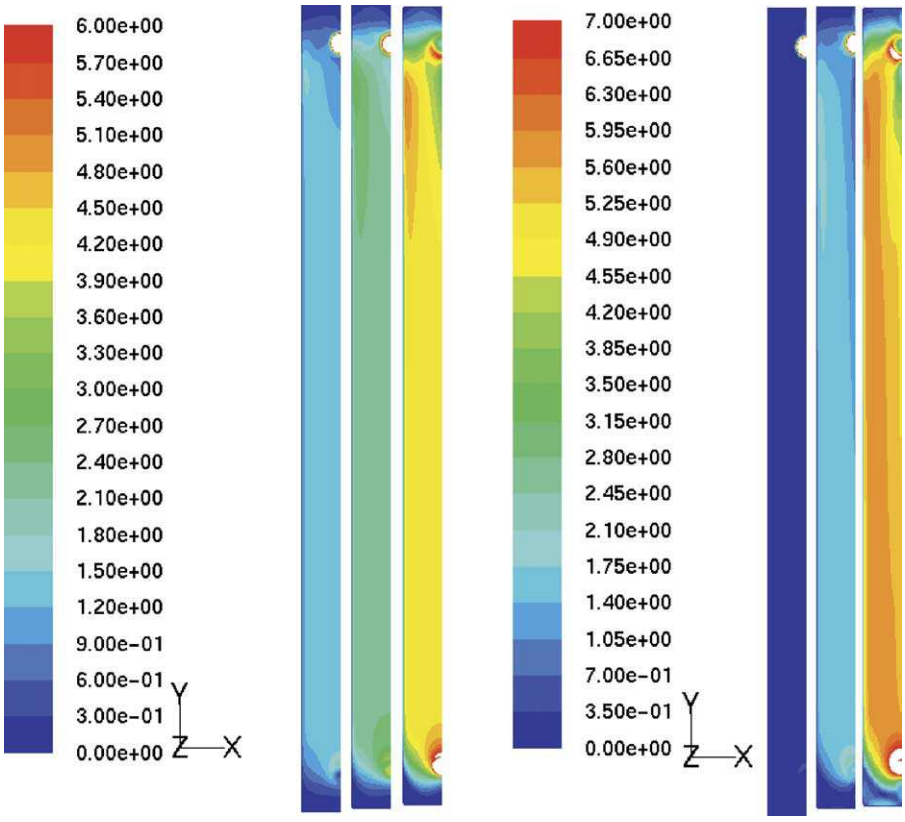

Fig. 6. Intra-channel flow distribution for oil and water, left and right, respectively, for an average cross flow velocity of 2 m/s, at the mid-gap of channels 5, 3 and 1, respectively.

5. Conclusions

The flow and pressure distributions in a plate and frame ultrafiltration module operating in Z configuration were compared using two predictive approaches; (a) a 1D solution using Bernoulli type energy balance and (b) a three-dimensional CFD solutions of the Navier-Stokes equations. Using the CFD solution as a benchmark, the 1D model predictions were improved by implementing several features which are novel to this work, namely:

- incorporation of a variable contraction co-efficient in the distributor orifice in a closed distributor–collector arrangement,
- the use of the 1/7th power law velocity profile in the distributor and collector,
- halving the effective orifice area of the 1D model based on particle tracing and velocity distributions observed in the CFD solutions at the collector and distributor.

The flow distributions obtained with the 1D model with the modified orifice compared very well with the CFD predictions. Pressure distributions were qualitatively predicted, but the 1D model was typically 30% lower than the CFD values. The main advantage of the 1D model was the virtually instant generation of results and the minimal amount of effort required to modify the geometry of the module. Future work will use the 1D model to screen module design changes before verification with the CFD solutions.

Significant inter-channel flow maldistribution was predicted with both models. The mean flow rate increased monotonically with channel number in all cases and the maldistribution worsened with increasing design cross flow velocity. The maldistribution ratio, κ, increased from 2.0 to 6.9 with increasing mean cross flow velocities of 0.5–5 m/s when using oil as the feed. Using water as a feed increased κ from 9.6 to 20.6 for the same range of cross flow velocities, primarily due to the reduced pressure equilibration provided by the losses in the channel flow.

Velocity reductions along the distributor generated pressure increases at the end of a bank while the inverse occurred along the collector. These two pressure distributions coupled to generate an increasing pressure drop across the channels with increasing channel number, biasing flow to the final channel.

Acknowledgements

The authors would like to thank: Ron Jerome of Chemical Systems Analysis, ICPET, NRCC, for help with computational aspects related to the CFD work and Peter A. Strakey for helpful correspondence regarding the variable contraction co-efficient.

Nomenclature

A	area (m^2)
C_c	contraction co-efficient (−)
d	orifice diameter (m)
D_p	distributor/collector diameter (m)
e	orifice length (m)
h	channel gap (m)
k	turbulent kinetic energy (m^2/s^2)
L_p	plate thickness (m)
l	channel length (m)
P	pressure (Pa)
V	average fluid velocity (m/s)
w	channel width (m)

Greek letters

ϵ	turbulent dissipation rate (m^2/s^3)
μ	viscosity (kg/m/s)
ρ	density (kg/m^3)

Subscripts

c	collector
cc	fluid entering collector at outer annulus
co	collector orifice
cr	fluid existing in collector
d	distributor
dc	fluid leaving distributor outer annulus
dr	fluid remaining in distributor
do	distributor orifice

References

[1] A.K. Majumdar, Mathematical modelling of flows in dividing and combining flow manifold, Appl. Math. Modelling 4 (12) (1980) 424–432.

[2] P.J. Heggs, H.-J. Scheidat, Thermal performance of plate heat exchangers with flow maldistribution, HTD-Vol. 201, Compact Heat Exchangers for Power and Process Industries, ASME 1992. 87–93.

[3] M.F. Edwards, D.I. Ellis, M. Amooie-Foumeny, The flow distribution in plate heat exchangers, Heat Transfer, Vol. 1, The Institution of Chemical Engineers, Symposium Series 86 (1984) 1289–1302.

[4] R.J. Kee, P. Korada, K. Walters, M. Pavol, A generalized model of the flow distribution in channel networks of planar fuel cells, J. Power Sources 109 (2002) 148–159.

[5] C.-W. Chen, Y.-W. Shau, C.-P. Wu, Analogic modelling for systemic circulation, Biomed. Eng. Appl. Basis Commun. 8 (2) (1996) 145–150.

[6] J.E. Tsitlik, H.R. Halperin, A.S. Popel, A.A. Shoukas, F.C.P. Yin, N. Westerhof, Modeling the circulation with three-terminal electrical networks containing special nonlinear capacitors, Ann. Biomed. Eng. 20 (1992) 595–616.

[7] F. Toldy, A. Bitai, G. Lipovszki, P. Niedermayer, Checking and control of pipeline networks, Periodica Polytechnica Mech. Eng. 22 (4) (1978) 313–323.

[8] S.L. Ke, H.C. Ti, Transient analysis of isothermal gas flow in pipeline network, Chem. Eng. J. 76 (2000) 169–177.

[9] S.K. Karode, Laminar flow in channels with porous walls, revisited, J. Membr. Sci. 191 (2001) 237–241.

[10] P.A. Strakey, D.G. Talley, The effect of manifold cross-flow on the discharge coefficient of sharp-edged orifices, Atom. Sprays 9 (1) (1999) 51–68.

[11] K. Darcovich, F.N. Toll, F. Paynot, E. Pelerin, Inlet plenum pressure drop calculation for a cross-flow module, CJChE 77 (1999) 119–121.

[12] R.B. Bird, W.E. Steward, E.N. Lightfoot, Transport Phenomena, John Wiley, Sons, New York, 1960.

[13] J.M. Escobar, Mechanics of manifold flow, in: J.S. McNown (ed.), Classic Papers in Hydraulics, New York, 1982. 464–468.

[14] C.J. Geankopolis, Transport processes and unit operations, second ed., Allyn and Bacon, Boston, MA, 1983.

[15] R.H. Perry, D.W. Green, Perry's Chemical Engineers' Handbook, sixth ed., McGraw Hill Book Company, 1984.

[16] V. Yakhot, S.A. Orzag, Renormalization Group Analysis of Turbulence. I. Basic Theory, J. Sci. Comput. 1 (1986) 3–52.

[17] B.E. Launder, D.B. Spalding, Lectures in Mathematical Models of Turbulence, Academic Press, London, England, 1972.

[18] G.F. Jones, Heat transfer and flow distribution within radiant-convective finned-tube manifold assemblies, Ph.D. Thesis, University of Pennsylvania.

[19] M.C. Porter, Concentration polarization with membrane ultrafiltration, Ind. Eng. Chem. Prod. Res. Dev. 11 (1972) 234–248.